Journal of Alloys and Compounds 788 (2019) 891–896

Contents lists available at ScienceDirect

Journal of Alloys and Compounds

journal homepage: http://www.elsevier.com/locate/jalcom

Study the relation between band gap value and lattice constant of $MgTi_2O_4$

Yujun Shi [a], Jie Lian [a, *], Wei Hu [b], Yuxiang Liu [a], Ge He [b], Kui Jin [b], Haonan Song [a], Kai Dai [a], Jiaxiong Fang [c]

[a] School of Information Science and Engineering, Shandong University, Qingdao, 266237, Shandong, China
[b] National Lab for Superconductivity, Institute of Physics, Chinese Academy of Sciences, Beijing, 100190, China
[c] Advanced Research Center for Optics, Shandong University, Jinan, 250100, Shandong, China

ARTICLE INFO

Article history:
Received 31 October 2018
Received in revised form
21 February 2019
Accepted 23 February 2019
Available online 25 February 2019

Keywords:
$MgTi_2O_4$
Spectroscopic ellipsometry
Optical constants
Band gap

ABSTRACT

As an accurate technique, spectroscopic ellipsometry (SE) is utilized to study the dielectric function ($\varepsilon = \varepsilon_r + i\varepsilon_i$) of spinel oxide $MgTi_2O_4$ (MTO) thin films with good orientation. C-axis lattice length and Ti ions valence state are characterized by X-ray diffraction and X-ray photoelectron spectroscopy, respectively. Here, we find that c-axis lattice constants have the positive correlation with band gaps which are obtained by fitting the spectra of $d^2(E^2\varepsilon_i)/dE^2$ via standard critical points model in MTO, and this phenomenon can be revealed by the Ti ions valence state. Moreover, the band gap value of MTO measured by experiment is consistent with the result of first-principles calculations.

1. Introduction

Spinel oxides with AB_2O_4 structure are ranked as one of the richest groups. With different physical properties including spin fluctuations [1–3], charge ordering [4,5] and orbital ordering [6], spinel oxides with AB_2O_4 structure generate intriguing functionalities such as superconductivity [7], ferroelectricity [8,9], magnetostriction [9,10] and so on. Excepting these interesting physical properties, spinel oxides also exhibit wide applications in electronics, catalysis and electrochemical science such as batteries [11–13], fuel cells [14–16] and electrolysers [17]. As a typical correlated spinel oxide, $MgTi_2O_4$ (MTO) has been extensively investigated due to the special electric structure. In this compound, Ti ions are surrounded by six oxygens forming a TiO_6 octahedron. Ti-3d levels split to lower triply degenerate levels t_{2g} and higher doubly degenerate levels e_g under local cubic environment. In MTO, Ti^{3+} indicates a free electron in t_{2g} orbital, whereas a metal-insulator transition (MIT) along with cubic to tetragonal structure transition, happens at about 260 K, which has attracted many research groups to use transport measurements to explore its physical mechanism [18,19]. However, optical reports are far less than transport measurements. Actually, optical properties play an important role in studying novel materials and potential applications.

As one nondestructive optical method, spectroscopic ellipsometry (SE) technique measures the amplitude and phase information simultaneously. Thus, SE has become a suitable way to determinate the optical constants $N = n + ik$ or complex dielectric function $\varepsilon = \varepsilon_r + i\varepsilon_i$ [20,21], which don't need to convert data from other optical experimental data, such as reflectivity measurement. Generally, ε_i represents the loss of materials and through fitting the second derivative spectra of ε_i ($d^2(E^2\varepsilon_i)/dE^2$) can quantitively research the electronic structure via standard critical point (SCP) model [22]. Jiang et al. [23] have researched the optical transition of $CH_3NH_3PbI_3$ perovskite by the second derivative via SE.

As known to us, physical properties of materials are decided by lattice crystalline. As another hotspot, studying the relationship between lattice constants and physical properties of materials has widely attracted many researcher's attentions [24–26]. Especially, the length of c-axis lattice constant always affects the electronic structure. Very recently, Feng et al. [27] have given the positive correlation between T_{c0} (zero resistance superconducting critical temperature) and c-axis lattice constant in FeSe thin films.

It should be noted that previous researches of MTO are mostly

* Corresponding author.
E-mail address: opticsdu@163.com (J. Lian).

https://doi.org/10.1016/j.jallcom.2019.02.261
0925-8388/

polycrystalline powder, which cannot study deeply its physical features. However, we have fabricated the MTO thin films with single orientation on (00*l*)-oriented $MgAl_2O_4$ (MAO) substrates by pulsed laser deposition (PLD) technique, and thin films are differed by the pulsed laser energy during growth process. X-ray diffraction (XRD, D8ADVANCE), X-ray photoelectron spectroscopy (XPS, ThermoFisher SCIENTIFIC) and atomic force microscopy (AFM, Nanosurf) are employed to characterize their crystal structures, Ti ions valence state and surface morphology, respectively. C-axis lattice constants are calculated by Bragg's formula, and SE (GES5, SOPRA) is utilized to get the optical constants. The interband transition energy value is analyzed by SCP model. In addition, we use the first-principles calculations to confirm the band gap value for MTO. What's more, in the viewpoint of Ti ion valence state, the relationship between c-axis length and transition energy is uncovered.

2. Experimental and theoretical methods

2.1. Fabrication

In PLD technique, the wavelength of laser for fabricating MTO thin films is 248 nm that decides the single photon energy. However, the laser energy per pulse is determined by the quantity of photons. Therefore, in our work, the only variable is pulsed laser energy during synthesizing MTO samples. The detailed synthesis conditions are listed by Table 1.

2.2. Characterization

Lattice structure of MTO thin films are measured by XRD with X-ray wavelength $\lambda = 1.54$ Å owing to the fact that X-ray source is Cu $K_{\alpha 1}$. Commercial Jade software is utilized to calculate the c-axis lattice constants. XPS is used to determine the Ti ions valence state. Crystal grain surface topographies are characterized by AFM. SE with a rotating analyzer explores samples' optical properties at room temperature. To get smoother ellipsometric data, the spectral resolution is set to 5 nm in the 300–800 nm wavelength range at an incident angle of 75.07.

2.3. Theoretical calculations

Based on the density functional theory (DFT), we combine the first-principles calculations to research density of states (DOS) and band structure of MTO compound. The calculation results come from Cambridge Sequential Total Energy Package (CASTEP) code. Gradient approximation (GGA) is used to deal with the exchange-correlation potential. According to the coverage test, a 400 eV energy cutoff is adopted for the plane wave expansion of the electronic wave function, and a $2 \times 4 \times 4$ Monkhorst-Pack grid is employed over the Brillouin zone [28–30].

Table 1
Synthesis condition of MTO thin films by PLD.

Sample name	Growth temperature (°C)	Pulsed laser energy (mJ)	Sputtering frequency (Hz)	Deposition time (min)
MTO_1	775	340	3	13
MTO_2	775	400	3	12
MTO_3	775	250	3	20

3. Results

3.1. Lattice structure and surface morphology

Fig. 1 displays the XRD 2θ spectra of MTO thin films grown on (00*l*)-oriented MAO substrates. The measuring range is 25–65°. (004) diffraction peaks of MTO and MAO are clearly arrowed in this pattern, which indicates single orientation and good epitaxy for all samples. The (004) diffraction peaks of MTO around 42.5° are enlarged in the inset. It can be distinctly observed that the difference of pulsed laser energy during growth makes the position of (004) diffraction peak vary, which demonstrates that the lattice constants change. This phenomenon of lattice constant as a function of pulsed laser energy is related by cation stoichiometry deviations [31].

Lattice constant of c-axis can be calculated by the Bragg's formula, and the values are listed in Table 2. From this Table, 8.4639 Å of MTO_1 is the longest one. Other study has pointed out that lattice constant of $MgTi_2O_4$ compound is 8.503 Å [32] where the Ti ions valence state is absolutely +3. Moreover, another work has reported that Ti ions valence state decreases as c-axis lattice constant increases [33]. Therefore, we consider the Ti ions valence state deviates +3 among MTO_1, 2 and 3, and meanwhile, MTO_1 possesses the lowest valence state of Ti ions as it owns the longest c-axis in our work.

Because Ti ions valence state is sensitive to c-axis lattice constant and changes with stoichiometry [34]. Thus, XPS technique is utilized to analyze the valence state of Ti ions, and Fig. 2 displays the binding energy of Ti 2p level. The green lines represent the peak maximum of Ti $2p_{3/2}$, which are 457.83, 458.26 and 458.59 eV for MTO_1, 2 and 3, respectively. These values are all lower than 458.70 eV of TiO_2 and higher than that of 457.40 eV in Ti_2O_3, indicating that the valence state of Ti ions is between +3 and + 4 [35]. According to the binding energy, MTO_1 owns the lowest Ti ions valence state and MTO_3 is the highest one.

AFM is a powerful tool for characterizing thin film surface

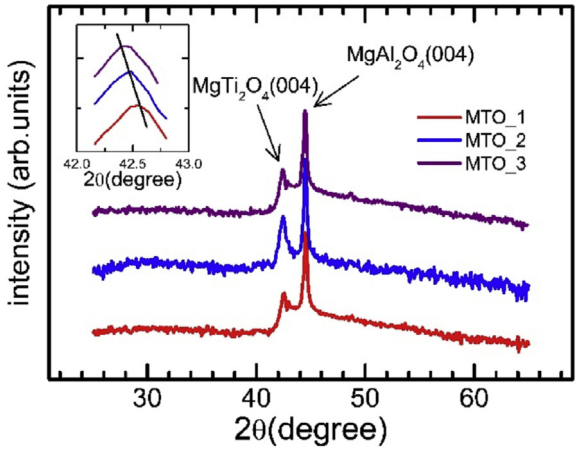

Fig. 1. The XRD patterns of MTO thin films grow on (00*l*)-oriented MAO substrates. Black arrows indicate the (004) diffraction peak of MTO and MAO.

Table 2
C-axis lattice constants of MTO thin films.

Sample name	c-axis lattice constant (Å)
MTO_1	8.4639
MTO_2	8.4509
MTO_3	8.4396

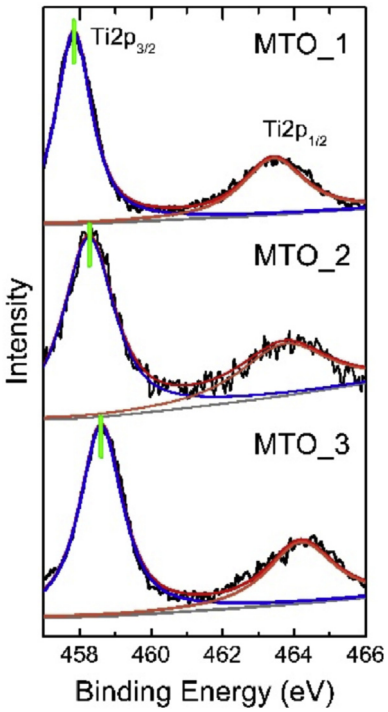

Fig. 2. XPS results of Ti 2p in MTO_1, 2 and 3. The green line is the peak maximum of Ti $2p_{3/2}$. (For interpretation of the references to colour in this figure legend, the reader is referred to the Web version of this article.)

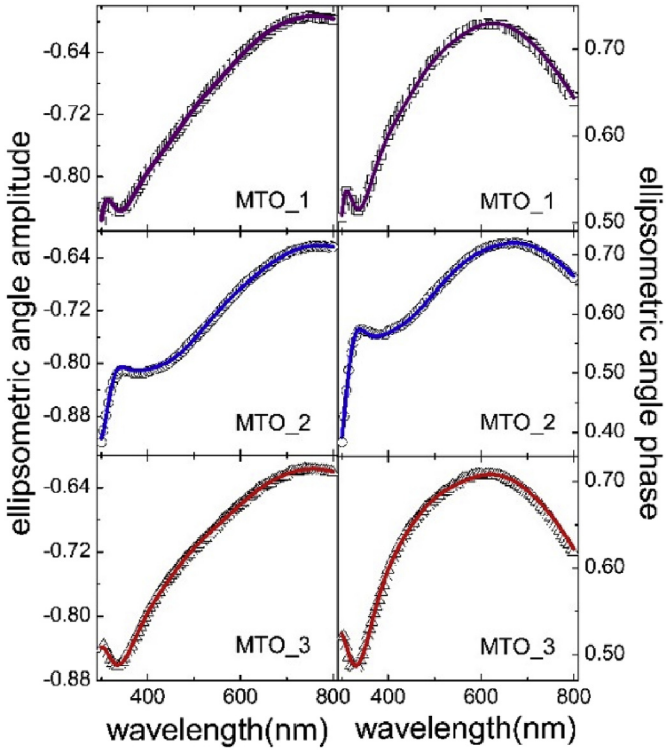

Fig. 4. Simulated (wine, blue and red solid lines) and experimental (hollow dots) ellipsometric angle amplitude and phase of MTO thin films. (For interpretation of the references to colour in this figure legend, the reader is referred to the Web version of this article.)

morphology. Fig. 3 displays the scanning images on $1 \times 1\ \mu m^2$ area. Homogeneous grains tightly arrange in the testing area, and smooth surface is clearly observed for MTO_1, 2 and 3, respectively. High quality samples open a credible door for systematic investigation of their optical properties.

3.2. Data of spectroscopic ellipsometry

Fig. 4 exhibits the simulated (solid lines) and experimental (hollow dots) data for ellipsometric angle amplitude and phase of the polarized reflected light from the surface of MTO thin films. According to AFM results, smooth surfaces are obtained. Thus, a three-layer model is built to express the optical structure (ambient/MTO/MAO substrate). Drude and three Lorentz oscillators are used to describe MTO-layer, and the same optical structure and dispersion law are utilized for these different lattice length samples. The Drude and Lorentz oscillator dispersion model are given by Table 3.

Where, P, D and E are the polarization, inverse of the plasma wavelength and mean free path respectively for Drude law. A, L_0 and γ are the intensity, central wavelength and width of absorption peak respectively for Lorentz oscillation. The best fitting parameters of Drude and Lorentz model are listed in Tables 4 and 5.

The film thickness is obtained to be 137.1 nm, 129.7 nm and 158.8 nm for MTO_1, 2 and 3, respectively. In the last, a consistent result between simulated and experimental data is achieved for all samples, see Fig. 4.

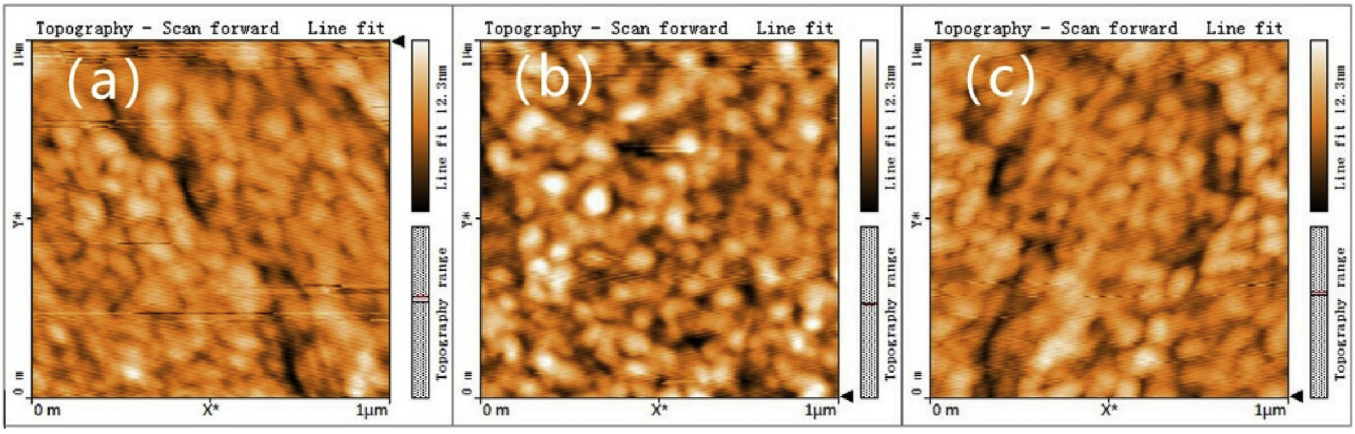

Fig. 3. AFM scanning images of MTO_1 (a), 2 (b) and 3 (c).

Table 3
Drude and Lorentz oscillator dispersion model.

Drude	Lorentz
$\varepsilon_r(\lambda) = P - D^2*\lambda^2/(1+(\lambda*E)^2)$	$\varepsilon_r(\lambda) = A*\lambda^2*(\lambda^2 - L_0^2)/[(\lambda^2 - L_0^2)^2 + \gamma^2*\lambda^2]$
$\varepsilon_i(\lambda) = E*D^2*\lambda^3/(1+(\lambda*E)^2)$	$\varepsilon_i(\lambda) = A*\lambda^3*\gamma/[(\lambda^2 - L_0^2)^2 + \gamma^2*\lambda^2]$

Table 4
The best fitting parameters for Drude dispersion model.

Sample name	P	D	E
MTO_1	2.75	1.79	0.23
MTO_2	0.94	1.53	0.16
MTO_3	2.59	1.55	0.24

Table 5
The best fitting parameters for Lorentz oscillator dispersion model.

Sample name	Peak 1			Peak 2			Peak 3		
	A	L_0	γ	A	L_0	γ	A	L_0	γ
MTO_1	1.37	0.24	0.03	0.57	0.42	0.29	3.08	0.20	0.03
MTO_2	2.10	0.96	0.67	1.38	0.25	0.02	2.73	0.99	0.73
MTO_3	0.37	0.41	0.22	1.57	0.96	0.53	0.34	0.42	0.23

4. Discussion

4.1. Optical properties and electronic transition energy of MTO

As seen in Fig. 5, it shows the dependence of refractive index n and extinction coefficient k on the photon energy of MTO. Refractive index n (see Fig. 5 (a)) increases with the incident photon energy. The inset is the Drude component which is extracted from dispersion law. Obviously, the real part of dielectric function (ε_r) of Drude model as Y-axis decreases towards the low photon energy in the inset, which indicates that these samples are typical metallic behavior at room temperature [36]. For extinction coefficient k (Fig. 5 (b)), small shoulders which are generally concerned with electronic transition energy as well as interband critical point energy (E_{cp}) appear around 2.8 eV for all samples. In addition, there exists an upturn above 3.75 eV. We suspect that there are other transition peaks exceed the testing range.

4.2. Theoretical calculation of electronic transition energy for MTO

Fig. 6 (a) and (b) are the band structure and the (DOS) of MTO,

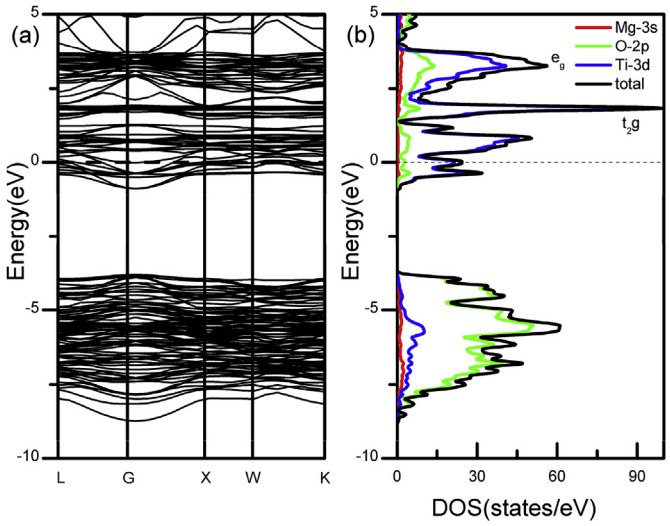

Fig. 6. (a) Band structure and (b) the density of state of MTO compound.

respectively. DOS is composed by the total density of states (TDOS) and the partial density of states (PDOS). As shown in Fig. 6 (b), Fermi level goes through the conduction bands, indicating that MTO is a metal material which is consistent with optical measurement. Based on the band theory, the outermost atomic levels (Mg: $3s^2$, Ti: $3d^24s^2$ and O:$2s^22p^4$) interact with each other. O-2p levels capture electrons to form lower energy valence band or higher energy conduction band, and Ti-3d levels form lower energy conduction band. Thus, the predominant contribution to TDOS derives from O-2p and Ti-3d levels, demonstrating the strong hybridization between O-2p and Ti-3d levels within the Ti-O octahedra. In addition, t_{2g} and e_g levels split by crystal field are obvious in Fig. 6 (b). Through the accurate calculations, the band gap between O-2p and Ti-3d levels is 2.6 eV.

4.3. In the view of Ti ions valence state to analyze electronic transition energies and understanding the relationship between c-axis lattice constants and band gaps of MTO

Fig. 7 (a), (b) and (c) exhibit the fitting results of $d^2(E^2\varepsilon_i)/dE^2$ dependence on photon energy that are performed by SCP analysis which can obtain accurately the quantitative values of band gap value, E_{cp}. The expression of SCP model is given by

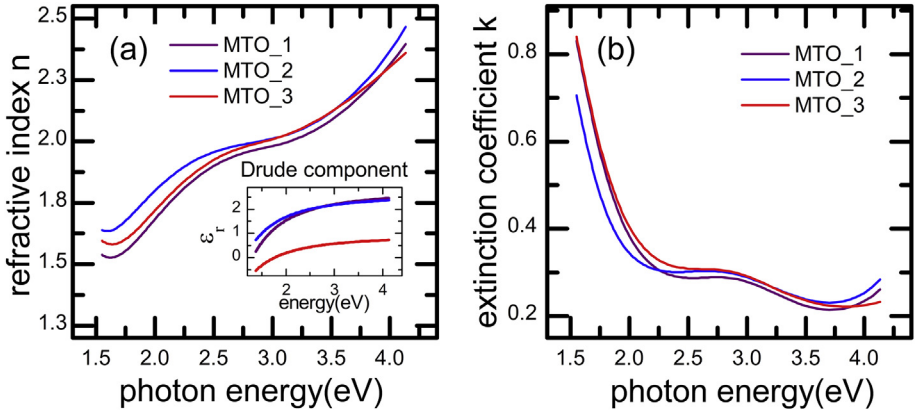

Fig. 5. (a) Refractive index n and (b) extinction coefficient k as a function of photon energy of MTO thin films. The inset in (a) shows the ε_r of Drude components which derived from the dispersion law.

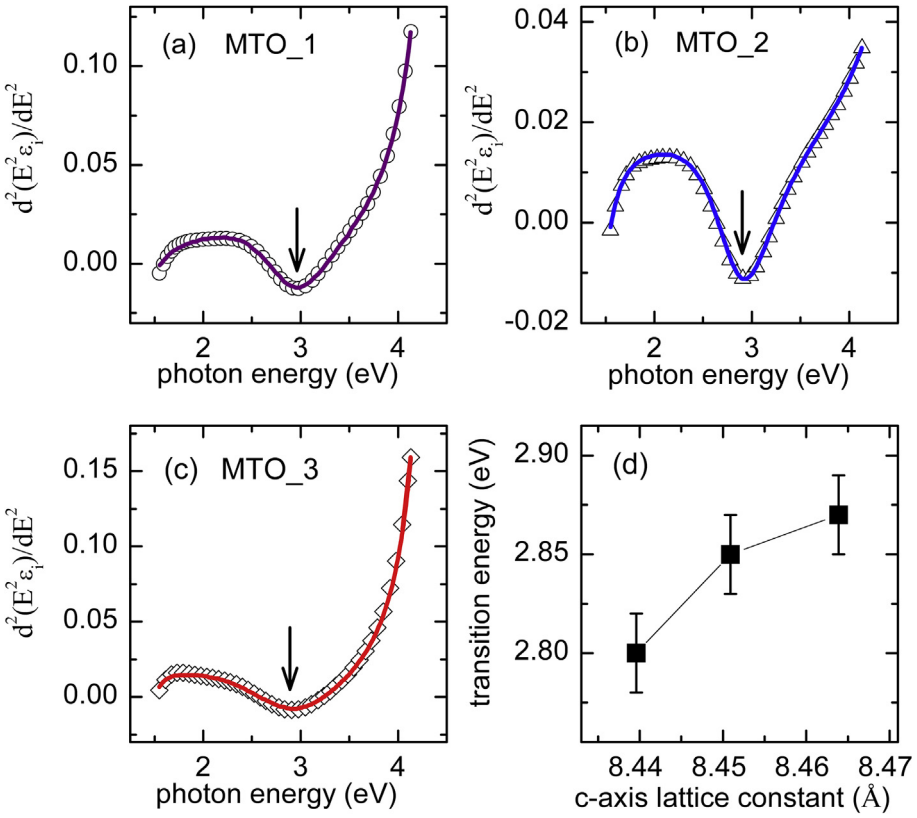

Fig. 7. (a), (b) and (c) are the second derivatives spectra of ε_i as a function of photon energy. The arrows indicate transition energy E_{cp}. (d) Relationship between transition energy values and c-axis lattice constants.

$$\frac{d^2(E^2\varepsilon)}{dE^2} = \begin{cases} n(n-1)Ae^{i\phi}(E - E_{cp} + i\Gamma)^{n-2}, & n \neq 0 \\ Ae^{i\phi}(E - E_{cp} + i\Gamma)^{-2}, & n = 0 \end{cases} \quad (1)$$

where A, ϕ, E and Γ represent the amplitude, excitonic phase angle, threshold energy and broadening parameter, respectively. Exponent n equals to 1/2, 0, −1/2 and −1 for three-, two-, one dimensionality and discrete excitons line shape. In our work, n is given to −1. The E_{cp} are 2.87 eV, 2.85 eV and 2.80 eV for MTO_1, 2 and 3, respectively. Fig. 7 (d) demonstrates the relationship between E_{cp} values and c-axis lattice constants.

Based on the results of XPS, we determine that MTO_1 possesses the smallest valence state of Ti. In this case, compared with other two samples, holes (positive charge) introduced into the system are the least one. Therefore, the hybridization between O-2p and Ti-3d level is the weakest as the Ti-3d level offer the least holes needed to be neutralized by O-2p electron. Thus, MTO_1 has the widest band gap which is associated with experiment result 2.87 eV. In this way, c-axis length should have the positive correlation with band gap. More surprisingly, the three samples we synthesis do follow this rule, and this conclusion are plotted in Fig. 7 (d). Moreover, we correlate material band gap with its lattice constant, which broaden SE potential application in terms of characterizing crystal structure.

4.4. Comparison the transition energy between MTO and Li_2TiO_4 (LTO) compound

The last but not least, we compare the electronic transition features of MTO and $LiTi_2O_4$ (LTO) compound. The reason to compare is that, on the one hand, the same spinel crystal structure and similar electronic structure are considered. On the other hand, inspired by the superconductivity with $T_c = 11$ K of Ti mixed-valent of LTO [24], MTO is also predicted to own 50 K superconductivity. Thus, they may possess the similar physical properties, such as orbital order.

Based on the previous theoretical calculation of electronic structure about LTO [29], the band gap between O-2p and Ti-3d level is 2.26 eV which is smaller than MTO. This phenomenon can also be explained by Ti ions valence state. +3.5 valence state is considered in LTO in theoretical calculation work, and holes of introducing to LTO system are more than MTO_1. Because MTO_1 is the closest one to +3 where the binding energy of 457.83 eV is very close to 457.4 eV in Ti_2O_3. Therefore, more holes are needed to neutralize by O-2p electrons in LTO than MTO_1. In this case, hybridization between O-2p and Ti-3d level in LTO would be stronger than MTO_1. Therefore, the band gap of LTO is less than MTO_1. It offers a clear reference for choosing an appropriate photoelectric device or potential battery materials [28,37,38] in the future.

5. Conclusions

In summary, we present a detailed study on lattice constants, Ti ions valence state, and dielectric functions of high quality MTO thin films. Due to the fact that different laser energy during deposition make the lattice constant change, we extract the positive correlation between lattice constants calculated by Bragg's formula and band gap values obtained by fitting the SCP model of $d^2(E^2\varepsilon_i)/dE^2$. This phenomenon can be well revealed by Ti ions valence state. Our results suggest that the valence state Ti ions plays a critical role on understanding the mechanism of the band gap value from O-2p to Ti-3d level in MTO system, which may further shed light on the potential properties of MTO, such as superconductivity. Meanwhile,

regulating band gap in MTO compound will be an underlying application in photoelectric detector.

Acknowledgments

This research was supported by the National Key Basic Research Program of China (No. 2015CB921003), and the Key Research and Development Project of Shandong Province (No. 2017GGX201008).

References

[1] K. Jin, G. He, X. Zhang, S. Maruyama, S. Yasui, R. Suchoski, J. Shin, Y. Jiang, H.S. Yu, J. Yuan, L. Shan, F.V. Kusmartsev, R.L. Greene, I. Takeuchi, Anomalous magnetoresistance in the spinel superconductor $LiTi_2O_4$, Nat. Commun. 6 (2015) 7183.

[2] H. Okabe, M. Hiraishi, A. Koda, K.M. Kojima, S. Takeshita, I. Yamauchi, Y. Matsushita, Y. Kuramoto, R. Kadono, Metallic spin-liquid-like behavior of LiV_2O_4, Phys. Rev. B 99 (2019), 041113.

[3] J.J. Melo Quintero, K.L. Salcedo Rodríguez, C.E. Rodríguez Torres, L.A. Errico, Ab initio study of the role of defects on the magnetic response and the structural, electronic and hyperfine properties of $ZnFe_2O_4$, J. Alloys Compd. 775 (2019) 1117–1128.

[4] P.G. Radaelli, Y. Horibe, M.J. Gutmann, H. Ishibashi, C.H. Chen, R.M. Ibberson, Y. Koyama, Y.S. Hor, V. Kiryukhin, S.W. Cheong, Formation of isomorphic Ir^{3+} and Ir^{4+} octamers and spin dimerization in the spinel $CuIr_2S_4$, Nature 416 (2002) 155–158.

[5] H. Ryoo, S.-G. Lee, J.-G. Kim, S.-Y. Chung, Effect of chemical bonding characteristics on ordering structure in Li spinel oxides, Adv. Funct. Mater. 29 (2019), 1805972.

[6] Y. Ishisuka, T. Ishisuka, R. Koborinai, T. Omura, T. Katsufuji, Comparative studies of the thermal conductivity of spinel oxides with orbital degrees of freedom, Phys. Rev. B 90 (2014), 224411.

[7] G. He, Y.L. Jia, X.Y. Hou, Z.X. Wei, H.D. Xie, Z.Z. Yang, J. Shi, J. Yuan, L. Shan, B.Y. Zhu, H. Li, L. Gu, K. Liu, T. Xiang, K. Jin, Anisotropic electron-phonon coupling in the spinel oxide superconductor $LiTi_2O_4$, Phys. Rev. B 95 (2017), 054510.

[8] Q. Zhang, K. Singh, F. Guillou, C. Simon, Y. Breard, V. Caignaert, V. Hardy, Ordering process and ferroelectricity in a spinel derived from FeV_2O_4, Phys. Rev. B 85 (2012), 054405.

[9] S.H. Lee, G. Tian, T.C. Kim, H.K. Jung, J.W. Choi, F.J. Walker, C.H. Ahn, C.A. Ross, D.H. Kim, Integration of sputter-deposited multiferroic $CoFe_2O_4$-$BiFeO_3$ nanocomposites on conductive $La_{0.7}Sr_{0.3}MnO_3$ electrodes, Nanotechnology 30 (2019), 105601.

[10] V. Kocsis, S. Bordacs, D. Varjas, K. Penc, A. Abouelsayed, C.A. Kuntscher, K. Ohgushi, Y. Tokura, I. Kézsmárki, Magnetoelasticity in ACr_2O_4 spinel oxides (A = Mn, Fe, Co, Ni, and Cu), Phys. Rev. B 87 (2013), 064416.

[11] Y. Sun, L. Zhao, H.L. Pan, X. Lu, L. Gu, Y.S. Hu, H. Li, M. Armand, Y. Ikuhara, L.Q. Chen, X.J. Huang, Direct atomic-scale confirmation of three-phase storage mechanism in $Li_4Ti_5O_{12}$ anodes for room-temperature sodium-ion batteries, Nat. Commun. 4 (2013) 1870.

[12] Y.Y. Sun, Y.H. Zou, F. Yuan, C.Y. Yan, S. Chen, Y.A. Jia, H.W. Zhang, D.J. Yang, X.L. She, Controllable synthesis of a peapod-like nanostructure via nano-confining $CoFe_2O_4$ in CMK-5 for high-performance lithium-ion batteries, Appl. Surf. Sci. 467–468 (2019) 640–647.

[13] T.L. Zhao, R. Ji, H.D. Yang, Y.X. Zhang, X.G. Sun, Y.T. Li, L. Li, R.J. Chen, Distinctive electrochemical performance of novel Fe-based Li-rich cathode material prepared by molten salt method for lithium-ion batteries, J. Energy Chem. 33 (2019) 37–45.

[14] C. Jin, F.L. Lu, X.C. Cao, Z.R. Yang, R.Z. Yang, Facile synthesis and excellent electrochemical properties of $NiCo_2O_4$ spinel nanowire arrays as a bifunctional catalyst for the oxygen reduction and evolution reaction, J. Mater. Chem. A 1 (2013) 12170.

[15] Y. Mouhib, M. Belaiche, S. Briche, C.A. Ferdi, E. Iffer, Elaboration, characterization and first principle studies of $MnCo_2O_4$ nanomaterials prepared from non-standard raw materials, Mater. Res. Express 6 (2018), 035508.

[16] K.T. Jacob, S. Sivakumar, Thermodynamic properties of $MgGa_2O_4$ and phase relations in the system Mg-Ga-O, J. Alloys Compd. 775 (2019) 1357–1364.

[17] C. Li, X.P. Han, F.Y. Cheng, Y.X. Hu, C.C. Chen, J. Chen, Phase and composition controllable synthesis of cobalt manganese spinel nanoparticles towards efficient oxygen electrocatalysis, Nat. Commun. 6 (2015) 7345.

[18] Y.Y. Zhu, R.J. Wang, L. Wang, Y. Liu, R. Xiong, J. Shi, M.L. Tian, Transition and transport behavior in spinel oxide $MgTi_2O_4$ and its La-doped counterparts, J. Alloys Compd. 666 (2016) 248–253.

[19] H.D. Zhou, J.B. Goodenough, Semiconductor-semiconductor transition in $Mg[Ti_2]O_4$, Phys. Rev. B 72 (2005), 045118.

[20] H.L. Liu, C.C. Shen, S.H. Su, C.L. Hsu, M.Y. Li, L.J. Li, Optical properties of monolayer transition metal dichalcogenides probed by spectroscopic ellipsometry, Appl. Phys. Lett. 105 (2014), 201905.

[21] H.L. Liu, M.K. Lin, Y.R. Cai, C.K. Tung, Y.H. Chu, Strain modulated optical properties in $BiFeO_3$ thin films, Appl. Phys. Lett. 103 (2013), 181907.

[22] S.Y. Li, S. Zamulko, C. Persson, N. Ross, J.K. Larsen, C. Platzer Björkman, Optical properties of $Cu_2ZnSn(S_xSe_{1-x})_4$ solar absorbers: spectroscopic ellipsometry and ab initio calculations, Appl. Phys. Lett. 110 (2017), 021905.

[23] Y.J. Jiang, A.M. Soufiani, A. Gentle, F.Z. Huang, A. Ho-Baillie, M.A. Green, Temperature dependent optical properties of $CH_3NH_3PbI_3$ perovskite by spectroscopic ellipsometry, Appl. Phys. Lett. 108 (2016), 061905.

[24] Y.L. Jia, G. He, W. Hu, H. Yang, Z.Z. Yang, H.S. Yu, Q.H. Zhang, J.N. Shi, Z.F. Lin, J. Yuan, B.Y. Zhu, L. Gu, H. Li, K. Jin, The effects of oxygen in spinel oxide $Li_{1+x}Ti_{2-x}O_{4-\delta}$ thin films, Sci. Rep. 8 (2018) 3995.

[25] H.S. Yu, J. Yuan, B.Y. Zhu, K. Jin, Manipulating composition gradient in cuprate superconducting thin films, Sci. China Phys. Mech. Astron. 60 (2017), 087421.

[26] X.L. Dong, H.X. Zhou, H.X. Yang, J. Yuan, K. Jin, F. Zhou, D.N. Yuan, L.L. Wei, J.Q. Li, X. Wang, G.M. Zhang, Z.Z. Zhao, Phase diagram of $(Li_{1-x}Fe_x)$OHFeSe: a bridge between iron selenide and arsenide superconductors, J. Am. Chem. Soc. 137 (2015) 66–69.

[27] Z.P. Feng, J. Yuan, G. He, W. Hu, Z.F. Lin, D. Li, X.Y. Jiang, Y.L. Huang, S.L. Ni, J. Li, B.Y. Zhu, X.L. Dong, F. Zhou, H.B. Wang, Z.X. Zhao, K. Jin, Tunable critical temperature for superconductivity in FeSe thin films by pulsed laser deposition, Sci. Rep. 8 (2018) 4039.

[28] Y.X. Liu, J. Lian, Y.J. Shi, H.N. Song, K. Dai, The first-principles calculations of $Mg_{2-x}Ti_{1+x}O_4$'s novel optical properties, J. Alloys Compd. 756 (2018) 57–61.

[29] Y.X. Liu, J. Lian, Z.Z. Sun, M.L. Zhao, Y.J. Shi, H.N. Song, The first-principles study for the novel optical properties of $LiTi_2O_4$, $Li_4Ti_5O_{12}$, $Li_2Ti_2O_4$ and $Li_7Ti_5O_{12}$, Chem. Phys. Lett. 677 (2017) 114–119.

[30] Y.X. Liu, J. Lian, X.L. Yang, M.L. Zhao, Y.J. Shi, H.N. Song, K. Dai, First-principles calculation for point defects in $Li_2Ti_2O_4$, Mater. Res. Express 4 (2017), 106502.

[31] S.A. Lee, H. Jeong, S. Woo, J.Y. Hwang, S.Y. Choi, S.D. Kim, M. Choi, S. Roh, H. Yu, J. Hwang, S.W. Kim, W.S. Choi, Phase transitions via selective elemental vacancy engineering in complex oxide thin films, Sci. Rep. 6 (2016) 23649.

[32] H. Hohl, C. Kloc, E. Bucher, Electrical and magnetic properties of spinel solid solutions $Mg_{2-x}Ti_{1+x}O_4$; $0 \leq x \leq 1$, J. Solid State Chem. 125 (1996) 216–223.

[33] M. Isobe, Y. Ueda, Synthesis, structure and physical properties of spinel solid solutions Mg_2TiO_4–$MgTi_2O_4$, J. Alloys Compd. 383 (2004) 85–88.

[34] A. Subba Rao, J. Ashok, B. Suresh, G. Naga Raju, N. Venkatramaiah, V. Ravi Kumar, I.V. Kityk, N. Veeraiah, Physical characteristics of $PbO–ZrO_2–SiO_2$:TiO_2 glass ceramics embedded with $Pb_2Ti_2O_6$ cubic pyrochlore crystal phase: Part-I electrical properties, J. Alloys Compd. 712 (2017) 672–686.

[35] J.W. Liu, H.T. Yuan, J.S. Cao, Y.J. Wang, Effect of Ti–Al substitution on the electrochemical properties of amorphous MgNi-based secondary hydride electrodes, J. Alloys Compd. 392 (2005) 300–305.

[36] M.L. Zhao, J. Lian, H.S. Yu, K. Jin, L.P. Xu, Z.G. Hu, X.L. Yang, S.S. Kang, Dielectric functions of La-based cuprate superconductors for visible and near-infrared wavelengths, Appl. Surf. Sci. 421 (2017) 611–616.

[37] K.P. Wu, K. Du, G.R. Hu, Red-blood-cell-like $(NH_4)[Fe_2(OH)(PO_4)_2]\cdot 2H_2O$ particles: fabrication and application in high-performance $LiFePO_4$ cathode materials, J. Mater. Chem. A 6 (2018) 1057–1066.

[38] Y.X. Liu, M.Y. Zhao, H. Xu, J. Chen, Fabrication of continuous conductive network for $Li_4Ti_5O_{12}$ anode by Cu-doping and graphene wrapping to boost lithium storage, J. Alloys Compd. 780 (2019) 1–7.